frontiers in Energy Research

ORIGINAL RESEARCH
published: 20 February 2019
doi: 10.3389/fenrg.2019.00011

Improving Photovoltaic Performance of ZnO Nanowires Based Colloidal Quantum Dot Solar Cells via SnO_2 Passivation Strategy

Shuhei Ozu[1], Yaohong Zhang[1], Hironobu Yasuda[1], Yukiko Kitabatake[1,2], Taro Toyoda[1], Masayuki Hirata[3], Kenji Yoshino[3], Kenji Katayama[2], Shuzi Hayase[4], Ruixiang Wang[5] and Qing Shen[1]**

[1] Faculty of Informatics and Engineering, University of Electro-Communications, Tokyo, Japan, [2] Department of Applied Chemistry, Chuo University, Tokyo, Japan, [3] Department of Electrical and Electronic Engineering, Miyazaki University, Miyazaki, Japan, [4] Faculty of Life Science and Systems Engineering, Kyushu Institute of Technology, Fukuoka, Japan, [5] Beijing Engineering Research Centre of Sustainable Energy and Buildings, Beijing University of Civil Engineering and Architecture, Beijing, China

OPEN ACCESS

Edited by:
Sergei Manzhos,
National University of Singapore,
Singapore

Reviewed by:
Zhijun Ning,
ShanghaiTech University, China
Jun Zhu,
Hefei University of Technology, China

***Correspondence:**
Yaohong Zhang
yhzhang1021@live.com
Qing Shen
shen@pc.uec.ac.jp

Specialty section:
This article was submitted to Solar Energy, a section of the journal Frontiers in Energy Research

Received: 08 December 2018
Accepted: 30 January 2019
Published: 20 February 2019

Citation:
Ozu S, Zhang Y, Yasuda H, Kitabatake Y, Toyoda T, Hirata M, Yoshino K, Katayama K, Hayase S, Wang R and Shen Q (2019) Improving Photovoltaic Performance of ZnO Nanowires Based Colloidal Quantum Dot Solar Cells via SnO_2 Passivation Strategy. Front. Energy Res. 7:11. doi: 10.3389/fenrg.2019.00011

Colloidal quantum dot solar cells (CQDSCs) based on one-dimensional metal oxide nanowires (NWs) as the electron transport layer (ETL) have attracted much attention due to their larger ETL/colloidal quantum dots (CQDs) contact area and longer electron transport length than other structure CQDSCs, such as planar CQDSCs. However, it is known that defect states in NWs would increase the recombination rate because of the high surface area of NWs. Here, the defect species on the ZnO NWs' surface which resulted in the surface recombination and SnO_2 passivation effects were investigated. Comparing with the solar cells using pristine ZnO NWs, the CQDSCs based on SnO_2 passivated ZnO NW electrodes exhibited a beneficial band alignment to charge separation, and the interfacial recombination at the ZnO/CQD interface was reduced, eventually resulting in a 40% improvement of power conversion efficiency (PCE). Overall, these findings indicate that surface passivation and the reduction of deep level defects in ETLs could contribute to improving the PCE of CQDSCs.

Keywords: colloidal quantum dot solar cells, PbS, ZnO nanowire, surface passivation, interfacial recombination, SnO_2

INTRODUCTION

Colloidal quantum dots (CQDs) have attracted immense attention due to their applications in the field of optoelectronic devices such as lasers (Hoogland et al., 2006), light-emitting diodes (Wood et al., 2009), and photovoltaic devices due to their bandgap tunability and solution processing (Mcdonald et al., 2005; Nozik et al., 2010; Zhang et al., 2012; Kagan et al., 2016). Colloidal quantum dot solar cells (CQDSCs), a promising contender for new-generation solar cells, have gained more and more attention (Brown et al., 2011; Zhang et al., 2014b, 2016, 2018; Carey et al., 2015; Wang et al., 2016; Hori et al., 2018). CQDs exhibit unique optical and electrical properties, such as an adjustable absorption spectrum and efficient multiple exciton generation (MEG) (Nozik, 2005). To date, the record power conversion efficiency (PCE) value of PbS-based CQDSCs is more than 12% (Xu et al., 2018).

In CQDSCs, CQDs work as an active (or a light absorbing) layer, and wide bandgap semiconductors (e.g., ZnO, TiO_2, etc.) are employed as an electron transport layer (ETL). In this architecture, a depletion region was formed near the ETL/CQD interface, which plays a very important role in charge separation and extraction (Choi et al., 2009; Willis et al., 2012). To absorb all incident light, the required thickness of the CQD layer is about 1 μm (Wang et al., 2015; Rekemeyer et al., 2016), but the total of depletion width (about 300 nm) and carrier diffusion length (about 100 nm) of PbS CQDSCs is presently only several hundred nanometers (Zhitomirsky et al., 2013). Thus, thickness of the PbS CQD layer is usually limited to about 500 nm even though the light absorption is not enough. Bulk heterojunction (BHJ) architecture is an effective design for solving this absorption-extraction compromise. The BHJ architecture of CQDSCs is beneficial for extending the depletion region and increasing the thickness of the CQD absorption layer (Barkhouse et al., 2011; Kramer et al., 2012), which can improve both optical absorption and charge collection. One-dimensional ZnO nanowires (NWs) have been used in BHJ CQDSCs (Wang et al., 2013; Chang et al., 2015; Rekemeyer et al., 2016; Zhang et al., 2017), and the record PCE of ZnO NW/PbS CQD-based CQDSCs has reached 9.6 % (Rekemeyer et al., 2016). However, this strategy would result in large interfacial charge recombination at the ZnO NW/CQD interface because of the high surface defect density of ZnO NWs (Ehrler et al., 2013; Choi et al., 2017; Cheng et al., 2018; Ding et al., 2018), in turn reducing the PCE of the CQDSCs. Thus, reducing the surface defect density of ZnO NWs is of critical importance for improving the photovoltaic performance of CQDSCs.

Surface passivation of ETL has proved to be an effective way to eliminate surface defects of ETL and inhibit interfacial recombination at the ETL/light absorber interface in various photovoltaic devices (Hori et al., 2018; Zang et al., 2018). In our previous work, thin amorphous TiO_2 was used as a passivation layer to cover the surface of ZnO NWs, and the interfacial charge recombination at the ZnO NW/CQD interface was attenuated in the CQDSCs (Chang et al., 2015). However, that work did not clarify which defect species of ZnO NWs was suppressed. Furthermore, how the variation of the surface defect state of ZnO NWs will influence the performance of CQDSCs has not been fully revealed.

Recently, SnO_2 has attracted attention not only as an ETL but also as a surface passivation material in solar cells, owing to its unique properties such as wide bandgap (∼3.6 eV), low chemical reactivity, high conductivity and good durability in ambient environment (Liu et al., 2016b; Khan et al., 2017; Wang et al., 2017). Herein we report the preparation of ZnO NW-based PbS CQDSCs and improve the PCEs of the CQDSCs from 5.6 to 7.8% through a thin amorphous SnO_2 surface passivation strategy. The type of defect states of the ZnO NWs was revealed, and we found that the surface defect density of ZnO NWs was reduced after being passivated by SnO_2. Due to the enhanced charge separation and reduced interfacial charge recombination efficiencies, the short-circuit current (J_{sc}), open-circuit voltage (V_{oc}) and fill factor (*FF*) of SnO_2 passivated ZnO (ZnO@SnO_2) NW-based CQDSCs largely improved more than that of the ZnO NW-based device, which corresponds to prolonging the effective carrier lifetime (τ_{eff}) in the former due to SnO_2 passivation. In addition, ZnO@SnO_2 NW-based CQDSCs can still work efficiently after being stored in air for more than 250 days. Our results indicate that SnO_2 surface passivation is an efficient way to improve the performance of ZnO NW-based CQDSCs.

MATERIALS AND METHODS

Synthesis of PbS CQDs

PbS CQDs were synthesized by our previous reported method (Zhang et al., 2017). Briefly, a mixed solution of 6 mmol PbO, 15 mmol oleic acid (OA) and 50 ml 1-ocatadecene (ODE) was vigorously stirred and vacuum degassed at room temperature for 30 min and at 100°C for 2 h, respectively. Finally, a clear lead oleate solution was obtained. Under nitrogen flow, 10 mL hexamethyldisilathiane (TMS)/ODE mixed solution (contained 3 mmol TMS) was rapidly injected into the already synthesized lead oleate solution at 100°C. After that, when the temperature of PbS colloid solution reduced to 75°C, a $CdCl_2$ precursor solution [contained 1 mmol $CdCl_2$, 0.1 mmol tetradecylphosphonic acid (TDPA), and 3 mL oleylamine (OLA)] was added into the above PbS solution. Finally, PbS CQDs were collected and purified by a toluene/acetone/methanol solution cleaning and centrifugation process. The PbS CQD precipitate was dried under an N_2 flow and finally dispersed in octane (60 mg mL^{-1}).

Growth of ZnO@SnO_2 NWs

Firstly, ZnO NWs were grown on FTO substrates by a similar method as shown in the literature (Chang et al., 2015). A Sn^{2+} precursor solution was prepared by dissolving 0.2 M $SnCl_2$ in ethanol and stirring at room temperature for about 30 min. Then, this Sn^{2+} precursor solution was dropped onto ZnO NW substrate and spun-cast at 4,000 rpm for 60 s. Finally, the passivated-ZnO NW substrate was heated at 150°C for 10 min and annealed at 400°C for 30 min in air.

Fabrication of PbS CQDSCs

The PbS CQD active layer was deposited onto the as-prepared NW substrate by a layer-by-layer method as shown in previously (Chang et al., 2015; Nakazawa et al., 2019). After the desired thickness of the PbS CQD layer was obtained, a thin layer of Au (∼100 nm) was deposited onto the PbS CQD layer by thermal evaporation as the metal electrode.

Characterization

Field-emission scanning electron microscope (FESEM) (JEOL, JSM-6340) and high-resolution transmission electron microscope (HRTEM) (JEOL, JEM- 2100F) techniques were applied to measure the lengths of the ZnO NW and thickness of SnO_2 passivation layer. X-ray photoelectron spectroscopy (*XPS*) (JEOL, S4 JPS-90MX) was used to measure the chemical state of elements, and photoelectron yield spectroscopy (PYS) spectra (Bunkoukeiki, BIP-KV205) were applied to determine the energy levels of NWs and CQDs. Photoluminescence (PL) spectra (JASCO, FP-6500) and UV-vis absorption spectra (HITACHI, U-3900H) were applied to measure the optical properties of NWs. The Hall effect was measured by using the

Van der Pauw method at room temperature (TOYO ResiTest 8300). The photocurrent density-voltage (*J-V*) measurements of PbS CQDSCs were conducted using a Peccell solar simulator PEC-L10 with a Keithley 2400 source meter. The transient photovoltage (TPV) decay measurements were performed by using a Nd:YAG laser (wavelength 532 nm) with a pulse duration of 5 ns and a pulse frequency of 4 Hz.

RESULTS AND DISCUSSION

Surface Passivation of ZnO NWs

After ZnO NW growth, SnO_2 layers were deposited onto the ZnO surface by spin-coating SnO_2 precursor containing $SnCl_2$. The SnO_2 layers were obtained through the hydrolysis and oxidation reaction of SnO_2 precursor in the following chemical equation (Marikkannan et al., 2015; Wang et al., 2017; Lu et al., 2018):

$$\begin{aligned} SnCl_2 + 2H_2O &\rightarrow Sn(OH)_2 + 2H^+ + 2Cl^- \\ Sn(OH)_2 &\rightarrow SnO + H_2O \\ 2SnO + O_2 &\rightarrow 2SnO_2 \end{aligned}$$

As shown in the above equation, the $SnCl_2$ which is absorbed on the surface of ZnO NWs firstly changed to $Sn(OH)_2$ through the hydrolysis reaction during or after the spin-coating process. It is worth noting here that the hydroxyl groups on the ZnO surface may benefit this reaction. Then, after annealing $Sn(OH)_2$ in open atmosphere, the SnO_2 layers were formed on the surface of ZnO NWs. Thus, the absorbed oxygen on the ZnO surface may be consumed when SnO_2 layers are formed. **Figure 1** shows a cross-sectional SEM image and TEM image of ZnO NWs with and without SnO_2 passivation. It can be clearly seen that the length of ZnO NWs is approximately 1 μm (see **Figure 1A**), and the morphology of NWs has no change after SnO_2 passivation (see **Figure 1B**). **Figures 1C,D** show the TEM images of ZnO NWs and ZnO@SnO_2 NWs, respectively. It can be found that the average diameter of ZnO NWs is about 40 nm and a thin amorphous SnO_2 layer coated the surface of ZnO NWs with a thickness of about 2 nm.

We employed *XPS* to investigate the composition and chemistry state of the surface of ZnO NWs and ZnO@SnO_2 NWs. As shown in **Figure 2A**, a characteristic peak of Sn $3d_{5/2}$ at 486.1 eV, which belongs to SnO_2, was detected in ZnO@SnO_2 NWs (Khan et al., 2017). It indicates that SnO_2 was deposited on the surface of ZnO NWs. The result is well-consistent with the TEM images. In **Figure 2B**, after fitting, the O 1s peak of ZnO NWs and ZnO@SnO_2 NWs can be divided into three peaks. The binding energy peaks assigned to the O^{2-} state in Metal oxides (O_M), oxygen vacancy or defects (O_D) and chemisorbed oxygen or hydroxyl groups (O_C) are observed at 529.5, 530.9, and 531.8 eV, respectively (Zhang et al., 2014a; Wang et al., 2017). We define the area of these peaks derived from O_M, O_D and O_C as S_M, S_D and S_C. The ratio of S_D/S_M and S_C/S_M roughly corresponds to the weight of each surface defect species in ZnO NWs (Azmi et al., 2016; Yang et al., 2018b). After calculation, we found that the ratio of S_D/S_M was almost the same (from 0.61 to 0.59) before and after SnO_2 passivation, but the ratio of S_C/S_M was significantly decreased (from 0.14 to 0.05) after SnO_2 passivation. These results indicate that the density of surface defects which corresponds to O_C was reduced; this is mainly because of the reduction of chemisorbed oxygen species or hydroxyl groups on the surface of ZnO NWs after forming the SnO_2 layer.

PL Spectra of ZnO NWs and ZnO@SnO_2 NWs

To further reveal the effect of the SnO_2 passivation layer, we measured PL spectra of ZnO NWs and ZnO@SnO_2 NWs at room temperature. The PL spectra of ZnO NWs and ZnO@SnO_2 NWs were fitted by using Gaussian functions for understanding the origins of various luminescent components as shown in **Figure 3**. After fitting, the PL spectra can be divided into seven peaks (Peak A-G) and the centers of those seven peaks are at 3.28 (Peak A), 3.21 (Peak B), 2.98 (Peak C), 2.62 (Peak D), 2.30 (Peak E), 2.17 (Peak F), and 2.03 eV (Peak G). The narrow emission peak in the ultraviolet region (Peak A) corresponding to the intrinsic near-band-edge transition of ZnO was observed in both ZnO NWs and ZnO@SnO_2 NWs as well. The origin of the violet-to-blue (Peak B, Peak C, and Peak D) region emission is attributed to vacancies or interstitials of zinc, and these defect species were reported to form the shallow level trapping states in ZnO (Djurišić et al., 2010; Vempati et al., 2012; Ding et al., 2018). Notably, the emission ranging from green (Peak E) to orange (Peak G) is assigned to oxygen-related defects that form deep level trapping states in ZnO, especially at the surface. Green (Peak E), yellow (Peak F), and orange (Peak G) emissions are caused by oxygen vacancy, hydroxyl groups, and excess oxygen, respectively (Studenikin et al., 1998; Djurišić et al., 2010; Panigrahy et al., 2010; Vempati et al., 2012; Zhang et al., 2014a). We can estimate the approximate surface defect density of ZnO from these emissions (Choi et al., 2017; Yang et al., 2018b). In **Figure 3A**, the PL intensity of green-to-orange (from Peak E to Peak G) emission clearly decreased after SnO_2 passivation on the ZnO NWs. This result indicates that the surface defect density of ZnO NWs was reduced after SnO_2 passivation. Furthermore, comparing the area of each PL emission spectrum related to different peaks of ZnO NWs and ZnO@SnO_2 NWs, it can be found that percentages of Peak E, Peak F, and Peak G are decreased after SnO_2 passivation (as shown in **Tables S1** and **Tables S2**). This is consistent with the result of *XPS* measurement, whereby the adsorbed oxygen species and hydroxyl groups on the surface of ZnO@SnO_2 NWs are lower than those of ZnO NWs. Therefore, SnO_2 passivation has the potential to suppress the charge recombination through deep level defect states of ZnO NWs, which originate from the absorbed oxygen and hydroxyl groups.

Energy Band Structure of ZnO@SnO_2 NWs

Surface passivation by SnO_2 not only has the potential to suppress interfacial recombination at the ZnO/CQD interface, but also affects the charge injection from CQDs to ZnO, so it is necessary to understand and select a favorable band alignment of ZnO and CQDs. First, we measured the absorption spectra of the ZnO NWs, ZnO@SnO_2 NWs, and PbS CQDs (see **Figure S1**). The optical band gaps (E_g) of both ZnO NWs and ZnO@SnO_2 NWs are about 3.29 eV (see **Figure 4A**), and the E_g of PbS

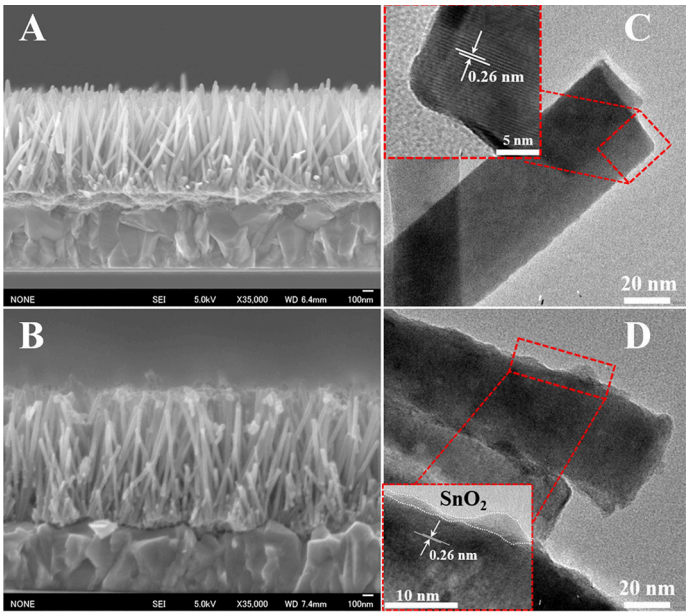

FIGURE 1 | The cross-sectional FESEM images of bare ZnO NWs **(A)** and ZnO@SnO_2 NWs **(B)**. TEM images of bare ZnO NWs **(C)** and ZnO@SnO_2 NWs **(D)**. The inset photograph is the HR-TEM image of NWs. TEM image of ZnO@SnO_2 NWs shows the surface of ZnO NWs covered with SnO_2 layer.

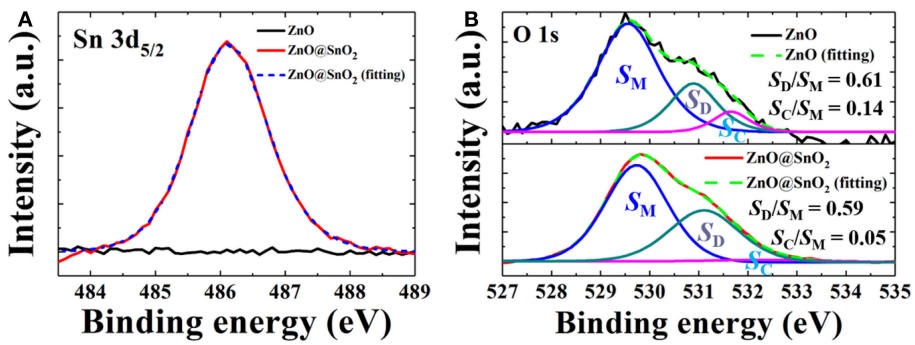

FIGURE 2 | *XPS* spectra of ZnO NWs and ZnO@SnO_2 NWs on glass: **(A)** Sn 3d and **(B)** O 1s with three resolved O bonding components (blue, green and pink lines).

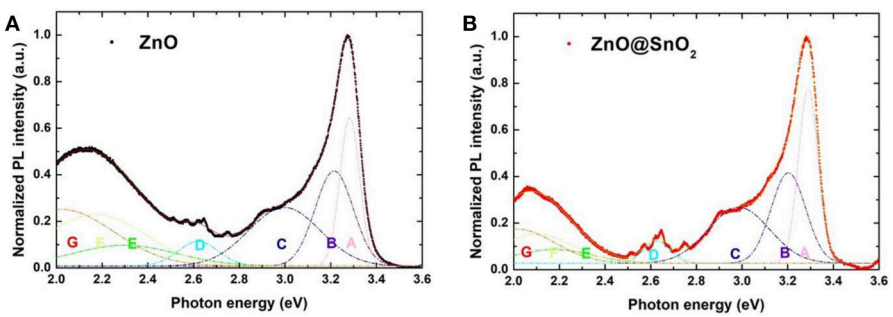

FIGURE 3 | PL spectra with several fitted emission peaks (from Peak A to Peak G): **(A)** ZnO NWs **(B)** ZnO@SnO_2 NWs.

CQDs is 1.25 eV (first exciton absorption peak is at 979 nm) (see **Figure S2**). Secondly, the valence band maximum (VBM) of ZnO NWs, ZnO@SnO_2 NWs, and PbS CQDs was measured by PYS technique (see **Figure 4B** and **Figure S3**). The VBM values of ZnO NWs, ZnO@SnO_2 NWs, and PbS CQDs, which are determined by the intersection of the tangent line and

the baseline of the PY spectra, are −7.58, −7.59, and −5.14, respectively. Moreover, the conduction band minimum (CBM) of these three samples can be calculated (ZnO NWs: −4.29 eV, ZnO@SnO_2 NWs: −4.30 eV, PbS CQDs: −3.89 eV) from the E_g and VBM values. Finally, the energy band diagram including the Fermi level (E_F) of the ZnO NWs, ZnO@SnO_2 NWs and PbS CQDs was obtained, as shown in **Figure 4C**. We calculated E_F of the three samples from their carrier density, which were obtained from Hall effect measurement (as shown in **Table S3**). Herein, the effective mass of bulk ZnO ($m_e \approx 0.24\ m_0$) and PbS ($m_h \approx 0.075\ m_0$) were used for calculation (Brus, 1984; Prastowo et al., 2018). It can be seen that the E_F of ZnO@SnO_2 NWs (−4.38 eV) is a little higher than that of ZnO NWs (−4.46 eV), which is mainly due to the larger carrier density of ZnO@SnO_2 NWs. This indicates that the density of the deep level defect state in ZnO@SnO_2 NWs, of which the trapped electrons cannot be thermally excited at around room temperature, has decreased compared to that in ZnO NWs. In addition, the upshift of E_F leads to an increasing of the depletion region width and V_{oc} in the CQDSCs; there is a possibility that ZnO@SnO_2 NWs have a more significant band bending (Liu et al., 2016a; Choi et al., 2017; Yang et al., 2018a), which may lead to an efficient charge separation at the ETL/CQD interfaces. Therefore, ZnO@SnO_2 NW-based CQDSCs have the potential to achieve a higher PCE than ZnO NW-based devices because of the improvement in charge separation efficiency and suppression of ZnO/CQD interfacial recombination.

Characterization and Photovoltaic Performance of ZnO@SnO_2 NWs Based CQDSCs

Figure 5 shows the schematic diagram of the architecture of CQDSCs and the *J-V* curves of the CQDSCs; their corresponding performance parameters are shown in **Table 1**. Cross-section SEM imaging of the ZnO@SnO_2 NW/PbS CQD/Au CQDSCs is shown in **Figure S3**. Compared to the ZnO NW-based device, ZnO@SnO_2 NW-based CQDSCs significantly exhibit superior performance. The deposition cycle of the SnO_2 layer was optimized and the device based on 2 deposition cycle of SnO_2 exhibits the best performance (see **Figure S4**). As expected from

TABLE 1 | Performance detail of the ZnO NW-based CQDSCs with and without SnO_2 passivation layer[a].

Devices	J_{sc} (mA/cm^2)	V_{oc} (V)	*FF*	*PCE* (%)
Without SnO_2	20.1 ± 0.3 (20.4)	0.558 ± 0.040 (0.580)	0.46 ± 0.01 (0.47)	5.23 ± 0.28 (5.55)
With SnO_2	23.2 ± 0.7 (23.2)	0.598 ± 0.006 (0.603)	0.53 ± 0.02 (0.56)	7.49 ± 0.27 (7.78)

All devices were measured under AM1.5 G 100 mW/cm^2 irradiation in air. [a]Data into the parentheses are parameters of champion devices.

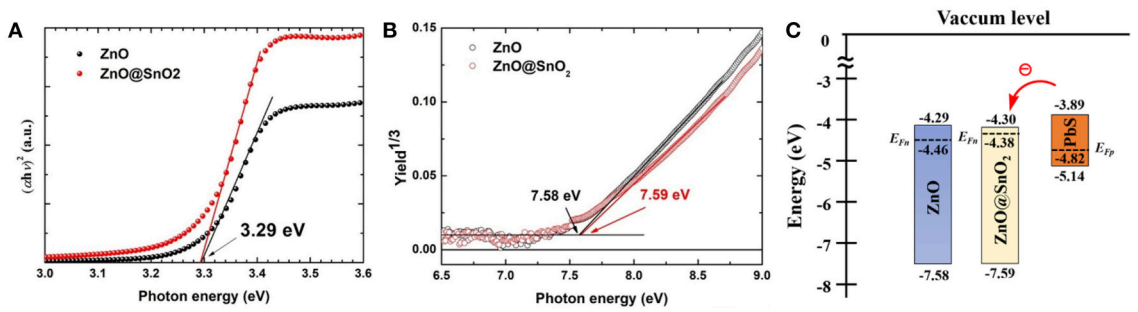

FIGURE 4 | (A) Tauc plots obtained from the absorption spectra of ZnO NWs and ZnO@SnO_2 NWs. **(B)** PYS spectra of ZnO NWs and ZnO@SnO_2 NWs. **(C)** Schematic energy band diagrams of ZnO NWs, ZnO@SnO_2 NWs, and PbS CQDs.

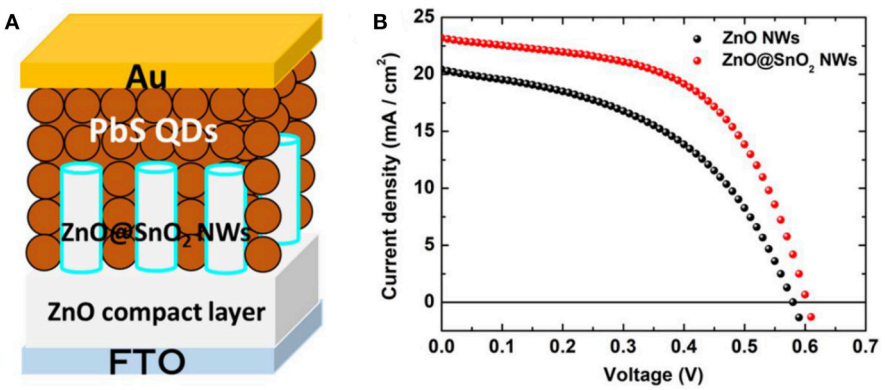

FIGURE 5 | (A) Schematic diagram of the architecture of ZnO@SnO_2 NW-based CQDSCs. **(B)** The *J-V* curves of ZnO NW CQDSCs with or without SnO_2 passivation.

the band alignment in the CQDSCs, the open-circuit voltage (V_{oc}) was improved due to the E_F upshift of ZnO@SnO_2 NWs and the reduced deep level defect density of ZnO. Meanwhile, enhancement of short-circuit current (J_{sc}) and fill factor (*FF*) of ZnO@SnO_2 NW-based CQDSCs can be explained by the improvement of charge separation and collection efficiencies, which were caused by the larger band bending and increased depletion region width. *IPCE* spectra of these devices supported this result (see **Figure S5**). Particularly, the *FF* of the ZnO@SnO_2 NW-based CQDSCs improved about 19% compared to that of the ZnO NW-based device, which confirms that the charge recombination was considerably suppressed. It is mainly caused by the reduction of surface defects on ZnO NWs and the reduced leakage current after SnO_2 passivation. Consequently, the PCE of ZnO@SnO_2 NW-based CQDSCs (7.8%) was enhanced about 39% more than that of the ZnO NW-based device (5.6%).

To investigate the detail of the charge recombination mechanism in ZnO NW CQDSCs, we have evaluated the diode ideality factor (n) of two types of CQDSCs (**Figure 6A**). As a reliable parameter of solar cells, the value of n can reflect the charge recombination process in CQDSCs. When interfacial recombination or trap-assisted recombination take over a majority in the recombination process, the value of n should be theoretically larger than unity ($1 < n < 2$) (Zhang et al., 2018). The light-intensity (P_{light}) dependence of the V_{oc} has the following relation:

$$V_{oc} \propto \frac{nkT}{q} \tag{1}$$

where n is the diode ideality factor, k is the Boltzmann constant, T is the temperature, and q is elementary charge (Cowan et al., 2010; Gao et al., 2014; Ding et al., 2018). By fitting the V_{oc} vs. light intensity plotted points, the values of n are determined to be 1.73 and 1.21 for ZnO NW-based CQDSCs and ZnO@SnO_2 NW-based devices, respectively (see **Figure 6A**). Interfacial recombination or trap-assisted recombination correlated with the deep level defect density in CQDSCs (Ding et al., 2018). In this work, the only difference between the two types of device is the presence or absence of SnO_2 passivation, so these results strongly confirm that ZnO/CQD interface charge recombination via deep level defect states of the ZnO NWs was suppressed after SnO_2 passivation. To further examine the charge recombination process in CQDSCs, we have measured transient photovoltage (TPV) decay. **Figure S6** shows the TPV decay curves of ZnO NW CQDSCs with and without SnO_2 passivation. TPV decay of ZnO@SnO_2 NW-based CQDSCs is slower than that of ZnO NW-based CQDSCs, which confirms that the charge recombination in ZnO@SnO_2-based devices was weakened. We also investigated the effective carrier lifetime (τ_{eff}) in CQDSCs, and τ_{eff} can be defined by the following equation:

$$\tau_{eff} = -\frac{\left(\frac{kT}{q}\right)}{\left(\frac{dV_{oc}}{dt}\right)} \tag{2}$$

Here, k is the Boltzmann constant, T is the temperature, and q is elementary charge (Zaban et al., 2003; Zhang et al., 2016). As shown in **Figure 6B**, it shows that the τ_{eff} of the CQDSCs was significantly increased after SnO_2 passivation, especially at high voltage regions (over 0.25 V). This result demonstrates that the charge recombination rate, which is the reciprocal of the carrier lifetime, of the ZnO@SnO_2 NW-based device decreased in the fast decay process. This result further confirms that SnO_2 passivation can significantly attenuate the charge

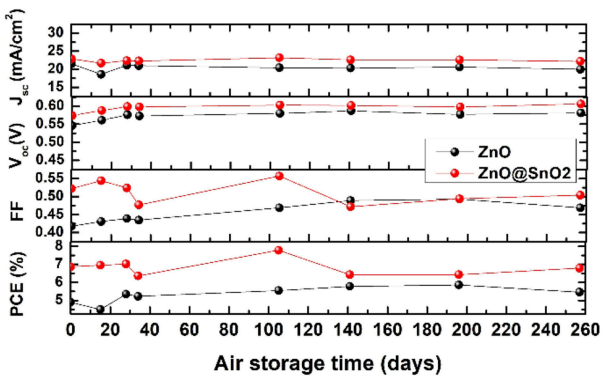

FIGURE 7 | Stability evaluations of ZnO NWs and ZnO@SnO_2 NWs based CQDSCs.

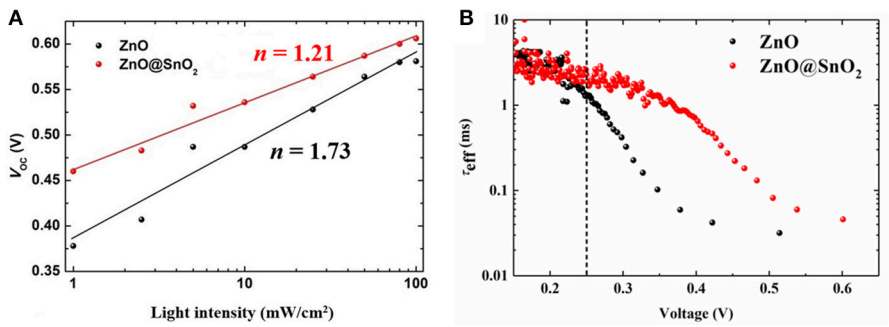

FIGURE 6 | (A) Light-intensity dependence of V_{oc} for CQDSCs with and without SnO_2 passivation. The solid black and red lines are the fitting curves. **(B)** τ_{eff} of CQDSCs with or without SnO_2 passivation that was calculated from the TPV decay curves of the devices which were shown in **Figure S6**.

recombination at the ZnO NW/CQD interface, and then enhance the performance of the devices, such as V_{oc}, *FF*, and PCE.

For CQDSCs, stability is important as well as PCE. Thus, the long-term stability of those devices was also evaluated, resulting in them being stored under ambient condition over half year. Both ZnO NW- and ZnO@SnO_2 NW-based CQDSCs exhibit excellent stable properties after being stored in air for 250 days, as shown in **Figure 7**. Therefore, it means that SnO_2 passivation can improve the PCE of CQDSCs while it does not impair the long-term stability of devices.

CONCLUSIONS

In summary, we used SnO_2 to passivate the surface of ZnO NWs and investigated the influence of SnO_2 passivation on the defect species of ZnO and the photovoltaic performance of the ZnO NW/PbS CQDSCs for the first time. We found that SnO_2 passivation can reduce the deep level defect density of the ZnO NWs, which is attributed to the absorbed oxygen and hydroxyl groups on the surface of ZnO NWs, and in turn reduces the surface recombination and leads to an upward shift of E_F. By SnO_2 passivation, the PCE of CQDSCs was improved from 5.6 to 7.8%. The SnO_2 passivation layer can effectively attenuate the charge recombination at the ZnO NW/CQD interface and increase the effective carrier lifetime in CQDSCs. More importantly, SnO_2 passivation enhanced the PCE of CQDSCs, while it does not impair the long-term stability of devices. Our study demonstrates that reducing the interfacial recombination at the ETL/CQD interface by using a wide bandgap semiconductor as a passivation layer is an effective way to enhance the performance of CQDSCs.

SUPPORTING INFORMATION

Fitting data of PL spectra; optical absorption spectra of ZnO NWs, ZnO@SnO_2 NWs, and PbS CQDs; PYS spectrum of PbS CQDs treated with CTAB; Absorption and IPCE spectra of devices; SnO_2 deposition cycle dependent photovoltaic performances of QDSCs; SEM image of CQDSCs; light-intensity dependence of J_{sc} for CQDSCs with and without SnO_2 passivation; TPV decay curves of ZnO NWs CQDSCs with and without SnO_2 passivation.

AUTHOR CONTRIBUTIONS

SO, YZ, and QS: conceived and designed the experiments; SO, HY, YK, and MH: performed the experiments; SO, YZ, TT, KK, and QS: analyzed the data; KY, SH, RW, and QS: contributed reagents, materials, analysis tools; SO: wrote the paper; YZ and QS: corrected the paper.

FUNDING

This work was supported by the Japan Science and Technology Agency (JST) CREST and PRESTO programs, Beijing Advanced Innovation Center for Future Urban Design, Beijing University of Civil Engineering and Architecture (Grant UDC2018031121), and the MEXT KAKENHI grant (Grands 26286013, 17H02736).

SUPPLEMENTARY MATERIAL

The Supplementary Material for this article can be found online at: https://www.frontiersin.org/articles/10.3389/fenrg.2019.00011/full#supplementary-material

REFERENCES

Azmi, R., Oh, S.-H., and Jang, S.-Y. (2016). High-efficiency colloidal quantum dot photovoltaic devices using chemically modified heterojunctions. *ACS Energy Lett.*1, 100–106. doi: 10.1021/acsenergylett.6b00070

Barkhouse, D. A., Debnath, R., Kramer, I. J., Zhitomirsky, D., Pattantyus-Abraham, A. G., and Levina, L. (2011). Depleted bulk heterojunction colloidal quantum dot photovoltaics. *Adv. Mater.* 23, 3134–3138. doi: 10.1002/adma.201101065

Brown, P. R., Lunt, R. R., Zhao, N., Osedach, T. P., Wanger, D. D., Chang, L. Y., et al. (2011). Improved current extraction from ZnO/PbS quantum dot heterojunction photovoltaics using a MoO3 interfacial layer. *Nano Lett.* 11, 2955–2961. doi: 10.1021/nl201472u

Brus, L. E. (1984). Electron–electron and electron-hole interactions in small semiconductor crystallites: the size dependence of the lowest excited electronic state. *J. Chem. Phys.* 80, 4403–4409. doi: 10.1063/1.447218

Carey, G. H., Abdelhady, A. L., Ning, Z., Thon, S. M., Bakr, O. M., and Sargent, E. H. (2015). Colloidal quantum dot solar cells. *Chem. Rev.* 115, 12732–12763. doi: 10.1021/acs.chemrev.5b00063

Chang, J., Kuga, Y., Mora-Ser,ó, I., Toyoda, T., Ogomi, Y., Hayase, S., et al. (2015). High reduction of interfacial charge recombination in colloidal quantum dot solar cells by metal oxide surface passivation. *Nanoscale* 7, 5446–5456. doi: 10.1039/C4NR07521H

Cheng, J. J., Chuang, C.-H. M., Hentz, O., Rekemeyer, P. H., Bawendi, M. G., and Gradečak, S. (2018). Dimension- and surface-tailored ZnO nanowires enhance charge collection in quantum dot photovoltaic devices. *ACS Appl. Energy Mater.* 1, 1815–1822. doi: 10.1021/acsaem.8b00204

Choi, J., Kim, Y., Jo, J. W., Kim, J., Sun, B., Walters, G., et al. (2017). Chloride passivation of ZnO electrodes improves charge extraction in colloidal quantum dot photovoltaics. *Adv. Mater.* 29:1702350. doi: 10.1002/adma.201702350

Choi, J. J., Lim, Y. F., Santiago-Berrios, M. B., Oh, M., Hyun, B. R., Sun, L., et al. (2009). PbSe nanocrystal excitonic solar cells. *Nano Lett.* 9, 3749–3755. doi: 10.1021/nl901930g

Cowan, S. R., Roy, A., and Heeger, A. J. (2010). Recombination in polymer-fullerene bulk heterojunction solar cells. *Phys. Rev. B* 82:245207. doi: 10.1103/PhysRevB.82.245207

Ding, C., Zhang, Y., Liu, F., Kitabatake, Y., Hayase, S., Toyoda, T., et al. (2018). Understanding charge transfer and recombination by interface engineering for improving the efficiency of PbS quantum dot solar cells. *Nanoscale Horizons* 3, 417–429. doi: 10.1039/C8NH00030A

Djurišić, A. B., Ng, A. M. C., and Chen, X. Y. (2010). ZnO nanostructures for optoelectronics: material properties and device applications. *Progr. Q. Electron.* 34, 191–259. doi: 10.1016/j.pquantelec.2010.04.001

Ehrler, B., Musselman, K. P., Böhm, M. L., Morgenstern, F. S., Vaynzof, Y., Walker, B. J., et al. (2013). Preventing interfacial recombination in colloidal quantum dot solar cells by doping the metal oxide. *ACS Nano* 7, 4210–4220. doi: 10.1021/nn400656n

Gao, F., Li, Z., Wang, J., Rao, A., Howard, I. A., Abrusci, A., et al. (2014). Trap-Induced Losses in Hybrid Photovoltaics. *ACS Nano* 8, 3213–3221. doi: 10.1021/nn501185h

Hoogland, S., Sukhovatkin, V., Howard, I., Cauchi, S., Levina, L., and Sargent, E. H. (2006). A solution-processed 1.53 μm quantum dot laser with

temperature-invariant emission wavelength. *Optics Express* 14, 3273–3281. doi: 10.1364/OE.14.003273

Hori, K., Zhang, Y., Tusamalee, P., Nakazawa, N., Yoshihara, Y., Wang, R., et al. (2018). Interface passivation effects on the photovoltaic performance of quantum dot sensitized inverse opal TiO2 solar cells. *Nanomaterials* 8:460. doi: 10.3390/nano8070460

Kagan, C. R., Lifshitz, E., Sargent, E. H., and Talapin, D. V. (2016). Building devices from colloidal quantum dots. *Science* 353:aac5523. doi: 10.1126/science.aac5523

Khan, J., Yang, X., Qiao, K., Deng, H., Zhang, J., Liu, Z., et al. (2017). Low-temperature-processed SnO_2-Cl for efficient PbS quantum-dot solar cells via defect passivation. *J. Mater. Chem. A* 5, 17240–17247. doi: 10.1039/C7TA05366E

Kramer, I. J., Zhitomirsky, D., Bass, J. D., Rice, P. M., Topuria, T., Krupp, L., et al. (2012). Ordered nanopillar structured electrodes for depleted bulk heterojunction colloidal quantum dot solar cells. *Adv. Mater.* 24, 2315–2319. doi: 10.1002/adma.201104832

Liu, M., de Arquer, F. P., Li, Y., Lan, X., Kim, G. H., Voznyy, O., et al. (2016a). Double-sided junctions enable high-performance colloidal-quantum-dot photovoltaics. *Adv. Mater.* 28, 4142–4148. doi: 10.1002/adma.201506213

Liu, Q., Qin, M.-C., Ke, W.-J., Zheng, X.-L., Chen, Z., Qin, P.-L., et al. (2016b). Enhanced stability of perovskite solar cells with low-temperature hydrothermally grown SnO_2 electron transport layers. *Adv. Functional Mater.* 26, 6069–6075. doi: 10.1002/adfm.201600910

Lu, S., Zhao, Y., Chen, C., Zhou, Y., Li, D., Li, K., et al. (2018). Sb_2Se_3 Thin-film photovoltaics using aqueous solution sprayed SnO_2 as the buffer layer. *Adv. Electron. Mater.* 4:1700329. doi: 10.1002/aelm.201700329

Marikkannan, M., Vishnukanthan, V., Vijayshankar, A., Mayandi, J., and Pearce, J. M. (2015). A novel synthesis of tin oxide thin films by the sol-gel process for optoelectronic applications. *AIP Adv.* 5:027122. doi: 10.1063/1.4909542

McDonald, S. A., Konstantatos, G., Zhang, S., Cyr, P. W., Klem, E. J., Levina, L., et al. (2005). Solution-processed PbS quantum dot infrared photodetectors and photovoltaics. *Nat. Mater.* 4:138. doi: 10.1038/nmat1299

Nakazawa, N., Zhang, Y., Liu, F., Ding, C., Hori, K., Toyoda, T., et al. (2019). The interparticle distance limit for multiple exciton dissociation in PbS quantum dot solid films. *Nanoscale Horizons*. doi: 10.1039/C8NH00341F. [Epub ahead of print].

Nozik, A. J. (2005). Exciton multiplication and relaxation dynamics in quantum dots: applications to ultrahigh-efficiency solar photon conversion. *Inorganic Chem.* 44, 6893–6899. doi: 10.1021/ic0508425

Nozik, A. J., Beard, M. C., Luther, J. M., Law, M., Ellingson, R. J., and Johnson, J. C. (2010). Semiconductor quantum dots and quantum dot arrays and applications of multiple exciton generation to third-generation photovoltaic solar cells. *Chem. Rev.* 110, 6873–6890. doi: 10.1021/cr900289f

Panigrahy, B., Aslam, M., Misra, D. S., Ghosh, M., and Bahadur, D. (2010). Defect-related emissions and magnetization properties of ZnO nanorods. *Adv. Functional Mater.* 20, 1161–1165. doi: 10.1002/adfm.200902018

Prastowo, S. H. B., Supriadi, B., Ridlo, Z. R., and Prihandono, T. (2018). Tunneling effect on double potential barriers GaAs and PbS. *J. Phys. Conference Series* 1008:012012. doi: 10.1088/1742-6596/1008/1/012012

Rekemeyer, P. H., Chang, S., Chuang, C.-H. M., Hwang, G. W., Bawendi, M. G., and Gradečak, S. (2016). Enhanced photocurrent in PbS quantum dot photovoltaics via ZnO nanowires and band alignment engineering. *Adv. Energy Mater.* 6:1600848. doi: 10.1002/aenm.201600848

Studenikin, S. A., Golego, N., and Cocivera, M. (1998). Fabrication of green and orange photoluminescent, undoped ZnO films using spray pyrolysis. *J. Appl. Phys.* 84, 2287–2294. doi: 10.1063/1.368295

Vempati, S., Mitra, J., and Dawson, P. (2012). One-step synthesis of ZnO nanosheets: a blue-white fluorophore. *Nanoscale Res. Lett.* 7:470. doi: 10.1186/1556-276X-7-470

Wang, H., Gonzalez-Pedro, V., Kubo, T., Fabregat-Santiago, F., Bisquert, J., Sanehira, Y., et al. (2015). Enhanced carrier transport distance in colloidal PbS quantum-dot-based solar cells using ZnO nanowires. *J. Phys. Chem. C* 119, 27265–27274. doi: 10.1021/acs.jpcc.5b09152

Wang, H., Kubo, T., Nakazaki, J., Kinoshita, T., and Segawa, H. (2013). PbS-quantum-dot-based heterojunction solar cells utilizing ZnO nanowires for high external quantum efficiency in the near-infrared region. *J. Phys. Chem. Lett.* 4, 2455–2460. doi: 10.1021/jz4012299

Wang, P., Zhao, J., Liu, J., Wei, L., Liu, Z., Guan, L., et al. (2017). Stabilization of organometal halide perovskite films by SnO_2 coating with inactive surface hydroxyl groups on ZnO nanorods. *J. Power Sources* 339, 51–60. doi: 10.1016/j.jpowsour.2016.11.046

Wang, R., Shang, Y., Kanjanaboos, P., Zhou, W., Ning, Z., and Sargent, E. H. (2016). Colloidal quantum dot ligand engineering for high performance solar cells. *Energy Environ. Sci.* 9, 1130–1143. doi: 10.1039/C5EE03887A

Willis, S. M., Cheng, C., Assender, H. E., and Watt, A. A., (2012). The Transitional heterojunction behavior of PbS/ZnO colloidal quantum dot solar cells. *Nano Lett.* 12, 1522–1526. doi: 10.1021/nl204323j

Wood, V., Panzer, M. J., Chen, J., Bradley, M. S., Halpert, J. E., Bawendi, M. G., et al. (2009). Inkjet-printed quantum dot-polymer composites for full-color AC-driven displays. *Adv. Mater.* 21, 2151–2155. doi: 10.1002/adma.200803256

Xu, J., Voznyy, O., Liu, M., Kirmani, A. R., Walters, G., Munir, R., et al. (2018). 2D matrix engineering for homogeneous quantum dot coupling in photovoltaic solids. *Nat. Nanotechnol.* 13, 456–462. doi: 10.1038/s41565-018-0117-z

Yang, F., Xu, Y., Gu, M., Zhou, S., Wang, Y., Lu, K., et al. (2018a). Synthesis of cesium-doped ZnO nanoparticles as an electron extraction layer for efficient PbS colloidal quantum dot solar cells. *J. Mater. Chem. A* 6, 17688–17697. doi: 10.1039/C8TA05946B

Yang, J., Lee, J., Lee, J., and Yi, W. (2018b). Suppressed interfacial charge recombination of PbS quantum dot photovoltaics by graphene incorporated into ZnO nanoparticles. *ACS Appl. Mater. Interfaces* 10, 25311–25320. doi: 10.1021/acsami.8b05556

Zaban, A., Greenshtein, M., and Bisquert, J. (2003). Determination of the electron lifetime in nanocrystalline dye solar cells by open-circuit voltage decay measurements. *Chem. Phys. Chem.* 4, 859–864. doi: 10.1002/cphc.200200615

Zang, S., Wang, Y., Li, M., Su, W., An, M., Zhang, X., et al. (2018). Performance enhancement of ZnO nanowires/PbS quantum dot depleted bulk heterojunction solar cells with an ultrathin Al_2O_3 interlayer. *Chinese Phys. B* 27:018503. doi: 10.1088/1674-1056/27/1/018503

Zhang, X., Qin, J., Xue, Y., Yu, P., Zhang, B., Wang, L., et al. (2014a). Effect of aspect ratio and surface defects on the photocatalytic activity of ZnO nanorods. *Sci. Rep.* 4:4596. doi: 10.1038/srep04596

Zhang, Y., Ding, C., Wu, G., Nakazawa, N., Chang, J., Ogomi, Y., et al. (2016). Air stable PbSe colloidal quantum dot heterojunction solar cells: ligand-dependent exciton dissociation, recombination, photovoltaic property, and stability. *J. Phys. Chem. C* 120, 28509–28518. doi: 10.1021/acs.jpcc.6b10920

Zhang, Y., Wu, G., Ding, C., Liu, F., Yao, Y., Zhou, Y., et al. (2018). Lead selenide colloidal quantum dot solar cells achieving high open-circuit voltage with one-step deposition strategy. *J. Phys. Chem. Lett.* 9, 3598–3603. doi: 10.1021/acs.jpclett.8b01514

Zhang, Y., Wu, G., Mora-Ser,ó, I., Ding, C., Liu, F., Huang, Q., et al. (2017). Improvement of photovoltaic performance of colloidal quantum dot solar cells using organic small molecule as hole-selective layer. *J. Phys. Chem. Lett.* 8, 2163–2169. doi: 10.1021/acs.jpclett.7b00683

Zhang, Y., Zhu, J., Liu, F., Wu, G., Wei, J., Hu, L., et al. (2014b). In_2S_3 sensitized solar cells with a new passivation layer. *J. Photochem. Photobiol. A Chem.* 281, 53–58. doi: 10.1016/j.jphotochem.2014.02.012

Zhang, Y., Zhu, J., Yu, X., Wei, J., Hu, L., and Dai, S. (2012). The optical and electrochemical properties of CdS/CdSe co-sensitized TiO_2 solar cells prepared by successive ionic layer adsorption and reaction processes. *Solar Energy* 86, 964–971. doi: 10.1016/j.solener.2012.01.006

Zhitomirsky, D., Voznyy, O., Hoogland, S., and Sargent, E. H. (2013). Measuring charge carrier diffusion in coupled colloidal quantum dot solids. *ACS Nano* 7, 5282–5290. doi: 10.1021/nn402197a

Conflict of Interest Statement: The authors declare that the research was conducted in the absence of any commercial or financial relationships that could be construed as a potential conflict of interest.